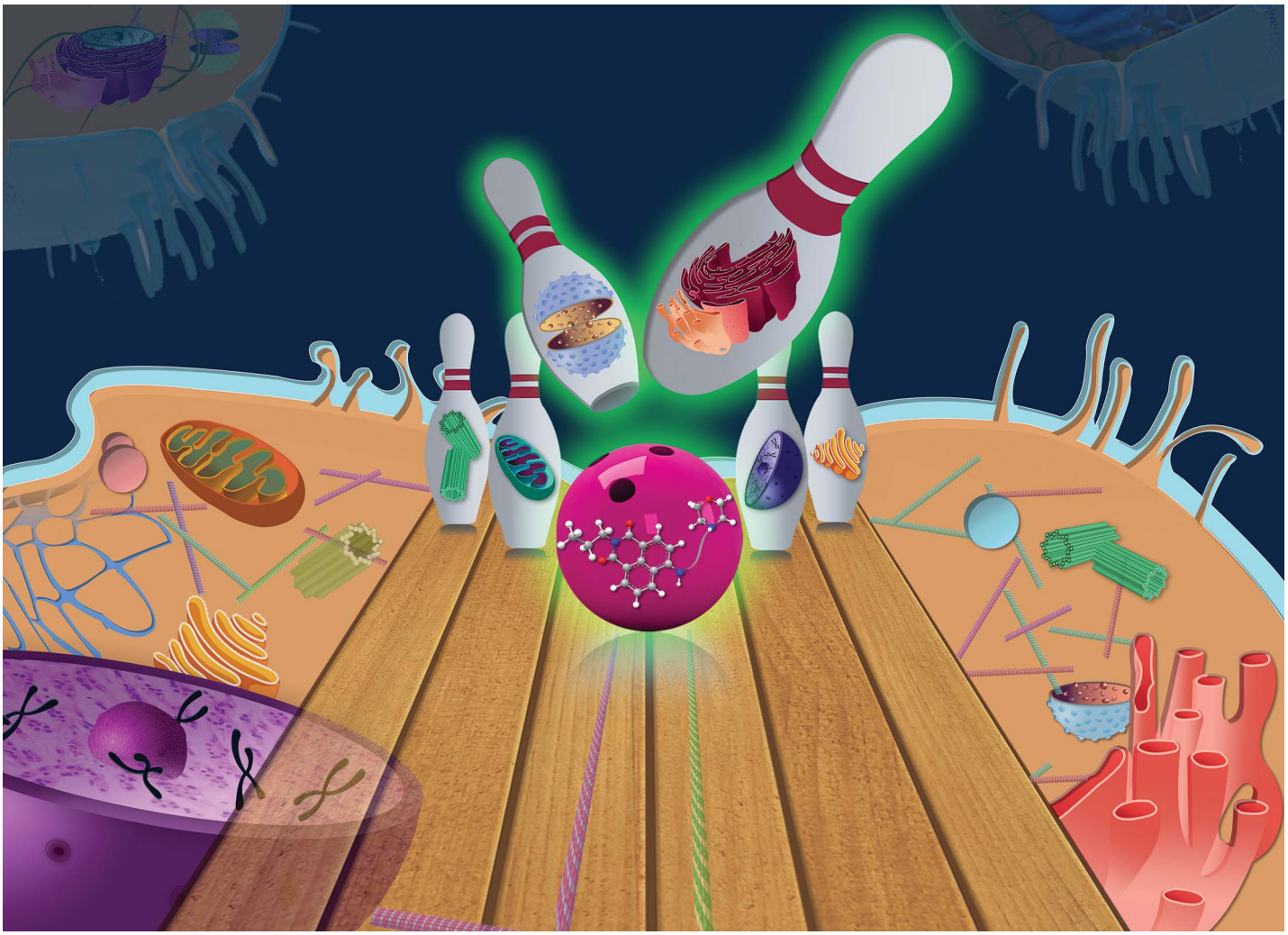

Showcasing research from Professor Apurba Lal Koner's and Professor Deepak Chopra's laboratories, Department of Chemistry, Indian Institute of Science Education and Research Bhopal (IISERB), Bhopal, Madhya Pradesh, India.

Strategic engineering of alkyl spacer length for a pH-tolerant lysosome marker and dual organelle localization

Dual organelle localization has been achieved by a 1,8-naphthalimide probe tethered with a long alkyl spacer terminated by a morpholine moiety. The long alkyl chain brings suitable lipophilicity to the probe effectuating the localization into the endoplasmic reticulum. Concurrently, lysosomal localization was observed owing to the attached morpholine moiety. Besides, this article also introduces an alkyl spacer length engineering strategy that helped us to understand the genesis of the pH tolerance. These findings are foreseen as building blocks to study lysosome-related dysfunctions and inter-organelle communication.

As featured in:

See Deepak Chopra, Apurba L. Koner *et al.*, *Chem. Sci.*, 2021, **12**, 9630.

ROYAL SOCIETY OF CHEMISTRY

rsc.li/chemical-science

Registered charity number: 207890

Chemical Science

ROYAL SOCIETY OF CHEMISTRY

EDGE ARTICLE

View Article Online
View Journal | View Issue

Cite this: *Chem. Sci.*, 2021, **12**, 9630

All publication charges for this article have been paid for by the Royal Society of Chemistry

Strategic engineering of alkyl spacer length for a pH-tolerant lysosome marker and dual organelle localization†

Suprakash Biswas,‡[a] Tanoy Dutta,‡[a] Akshay Silswal,[a] Rohit Bhowal,[b] Deepak Chopra *[b] and Apurba L. Koner *[a]

Long-term visualization of lysosomal properties is extremely crucial to evaluate diseases related to their dysfunction. However, many of the reported lysotrackers are less conducive to imaging lysosomes precisely because they suffer from fluorescence quenching and other inherent drawbacks such as pH-sensitivity, polarity insensitivity, water insolubility, slow diffusibility, and poor photostability. To overcome these limitations, we have utilized an alkyl chain length engineering strategy and synthesized a series of lysosome targeting fluorescent derivatives namely **NIMCs** by attaching a morpholine moiety at the *peri* position of the 1,8-naphthalimide (NI) ring through varying alkyl spacers between morpholine and 1,8-naphthalimide. The structural and optical properties of the synthesized **NIMCs** were explored by ^{1}H-NMR, single-crystal X-ray diffraction, UV-Vis, and fluorescence spectroscopy. Afterward, optical spectroscopic measurements were carefully performed to identify a pH-tolerant, polarity sensitive, and highly photostable fluoroprobes for further live-cell imaging applications. **NIMC6** displayed excellent pH-tolerant and polarity-sensitive properties. Consequently, all **NIMCs** were employed in kidney fibroblast cells (BHK-21) to investigate their applicability for lysosome targeting and probing lysosomal micropolarity. Interestingly, a switching of localization from lysosomes to the endoplasmic reticulum (ER) was also achieved by controlling the linker length and this phenomenon was subsequently applied in determining ER micropolarity. Additionally, the selected probe **NIMC6** was also employed in BHK-21 cells for 3-D spheroid imaging and in *Caenorhabditis elegans* (*C. elegans*) for *in vivo* imaging, to evaluate its efficacy for imaging animal models.

Received 28th January 2021
Accepted 13th June 2021

DOI: 10.1039/d1sc00542a

rsc.li/chemical-science

Introduction

Lysosomes are the most important membrane-bound cellular organelles in eukaryotic cells, frequently regarded as the cellular degradative compartment of the endocytic pathway.[1,2] The metabolic function of lysosomes proceeds through the disruption of various complex extracellular macromolecules into their constituent building blocks to regenerate nutrients, catalyzed by a group of proteases, lipases, nucleases, and other hydrolytic enzymes. The constituents are then transported to the cytoplasm *via* dedicated lysosomal membrane permeases.[3–8] To execute such catalytic propensity the hydrolases demand an acidic pH gradient of 4.5–5.5 and to maintain such a pH range, protons are pumped to the lysosomal interior from membrane-bound ATPase through ion-channels.[9,10] Besides, the acidic environment (pH 4.5–5.5) plays a crucial role in a variety of physiological processes, such as cellular homeostasis and plasma membrane repair.[11,12] Additionally, malfunction of various lysosomal hydrolases, proteases, and transporter enzymes caused by mutation of genes results in a gradual accumulation of undesired cargo inside lysosomes (lysosomal storage).[13] Over-accumulation of undesired substances inside the lysosomes can commence a cascade of secondary disorders which ultimately affects the pathway of calcium homeostasis, oxidative stress management, inflammatory immune response, and cell death.[14] As per example, the central nervous system expresses variable amounts of glycosphingolipid, and for this reason, some neuronal lysosomes allow this molecule to be stored and effectively released at a particular time. However, the

[a]*Bionanotechnology Lab, Department of Chemistry, Indian Institute of Science Education and Research Bhopal, Bhopal Bypass Road, Bhauri, Bhopal, Madhya Pradesh, India. E-mail: akoner@iiserb.ac.in*

[b]*Crystallography and Crystal Chemistry Laboratory, Department of Chemistry, Indian Institute of Science Education and Research Bhopal, Bhopal Bypass Road, Bhauri, Bhopal, Madhya Pradesh, India. E-mail: dchopra@iiserb.ac.in*

† Electronic supplementary information (ESI) available: The synthetic procedure and characterization (^{1}H, ^{13}C-NMR, HRMS) of **NIMCs**, pH- and solvent-dependent optical properties, variable temperature ^{1}H-NMR, cell viability assay for **NIMCs**, live-cell imaging for co-localization analysis, λ-scanning experiments for micropolarity determination, live-cell 3D spheroid imaging, crystal refinement parameters, and a table showing inter and intra-molecular interactions. CCDC 2053600–2053604. For ESI and crystallographic data in CIF or other electronic format see DOI: 10.1039/d1sc00542a

‡ These authors contributed equally to this work.

storage of these macromolecules by other neuronal lysosomes leads to neuronal damage and cell death.[13] Further, autophagosomes engulf intracellular constituents and consequently fuse with lysosomes promoting the formation of autolysosomes during autophagy.[15–20] Lysosomes and late endosomes frequently knot with other intracellular organelles such as mitochondria and endoplasmic reticulum, without fusing with them, and form functional membrane contact sites, which allow transfer of different lipid and protein composites between the organelles.[21] Hence, the transfer of such substances makes the lysosomal compartment dynamic in terms of its micro-environment, morphology, and spatial distribution.[13,22] Any disruption of such a dynamic balance may be a cause for diseases such as cardiovascular diseases, inflammation, and even cancer.[23–29] Research on lysosomal activity indicates that lysosomal polarity plays a pivotal role in their functionality and any unusual change in the lysosomal micro-polarity triggers significant disorder in apoptosis enabling uncontrolled cell death.[27,30–32] Recent experimental findings also indicate higher lysosomal micro-polarity in cancerous cells than in normal cells.[33,34] However, the dynamicity of lysosomal pH prohibits the use of various techniques for long-term visualization of their behavior. Therefore, convenient techniques are required to be developed for real-time monitoring of lysosomal activity, as well as their micro-polarity, to get an explicit vision of lysosome dysfunction-related diseases.[35,36]

The development of synthetic organic luminophores to stain biological samples for imaging applications is considered to be an extraordinary avenue in modern research trends. Organic fluoroprobe-based imaging techniques are often convenient to visualize specific regions of cells, model organisms, and biological processes, even with a few nanometer resolution, because of their excellent sensitivity and operational simplicity.[37,38] Due to the dynamicity of the lysosomal compartment, imaging lysosomal properties to comprehend their activities is extremely fascinating, and to pursue this, numerous synthetic organic lysotrackers have been reported by various research groups.[38–41] The majority of such reported lysosome targeting probes and commercially available lysotrackers such as Neutral Red (NR), DND-189, and DND-99 suffer from pH-dependent fluorescence, interference from non-specific binding, background fluorescence, insufficient photostability, and cytotoxicity.[26,42,43]

To target the most acidic organelle, that is, the lysosome, recently reported lysotrackers are designed to operate *via* the protonation of tertiary amine groups inside the lysosomal compartment.[38,44] For many such reported probes, the dynamicity and acidity of the lysosomal compartment impose limitations such as quenching of fluorescence intensity governed by the well-known phenomenon of photo-induced electron transfer (PET) or delocalization of the probe from lysosomes to elsewhere, resulting in non-specific targeting for long-term monitoring.[45] Recently, a few dextran conjugated lysosome-specific probes have been reported for understanding phagocytosis. However, these probes are less suitable for long-term imaging, as dextran itself interrupts the natural physiological activity of lysosomes.[46] Besides, the development of polarity sensitive fluoroprobes for monitoring the micro-environment of subcellular compartments is extremely essential for early-stage disease diagnosis.[47,48] Although very few lysosomal micro-polarity sensitive fluorescent probes have already been reported, their applicability in aspects such as differentiating between cancer cells/tissue and normal cells/tissue is less explored.[34,49] Additionally, vulnerable photostability and nonspecific background fluorescence outside the region of interest (ROI) of many probes are major limitations for imaging in fixed cells or static snapshots, without the possibility of continuous data acquisition for long-term tracking under a high-power LASER scanning confocal microscope (LSCM).[50,51] Therefore, the predicament demands a pH-tolerant, polarity sensitive, extremely photostable, non-toxic, and synthetically

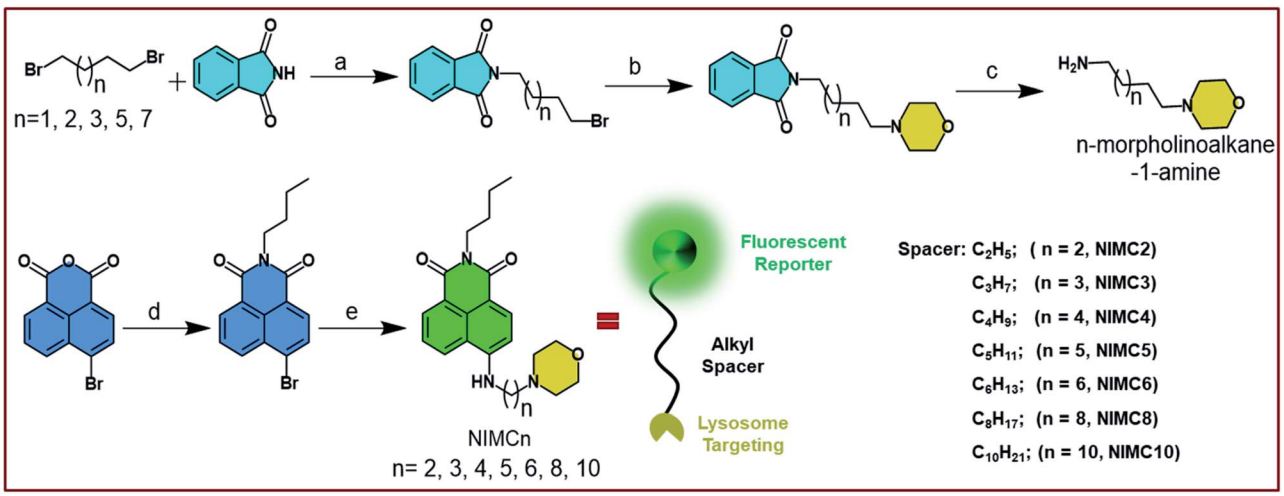

Scheme 1 Schematic representation of the synthesis of **NIMCs**, and the corresponding general conditions are as follows: (a) K_2CO_3, dry MeCN, reflux, 8 h, 78–83%; (b) morpholine, K_2CO_3, dry DMF, 100 °C, overnight, 84–91%; (c) $N_2H_4 \cdot H_2O$, EtOH, reflux, 2 h, quantitative yield; (d) *n*-butylamine, EtOH, reflux, 2 h, 77%; (e) *N*-morpholinoalkane-1-amine, dry DMSO, 105 °C, overnight, 51–57%.

simple lysosome targeting fluorescent marker for routinely monitoring lysosomal polarity.

Herein, we have addressed the limitation of fluorescence quenching with increasing pH due to PET and obtained a promising pH-tolerant lysotracker, afforded by a simple yet convenient synthetic approach.[52] Consequently, we have designed a series of fluoroprobes namely **NIMCs** (Scheme 1) by a simple alkyl chain length variation strategy and synthesized them by attaching a morpholine moiety at the *peri* position of the 1,8-naphthalimide (NI) ring through various alkyl spacers. The synthesized molecules were characterized by ^{1}H, ^{13}C-NMR spectroscopy, mass spectrometry, and single-crystal X-ray analysis. Afterward, a detailed spectroscopic investigation was conducted to comprehend the photophysical properties of all **NIMCs** in an aqueous medium. Further, the **NIMCs** were screened to evaluate their pH-tolerant fluorescence properties where **NIMC6** exhibited superior pH-tolerant fluorescence compared to other **NIMCs**. Moreover, the solvatochromic properties of all the **NIMCs** were probed, which demonstrates a conducive agreement between solvent polarity and solvatochromism. The **NIMCs** were subjected to live-cell imaging in BHK-21 cells where **NIMC2–6** were found to be localized exclusively in the lysosomal compartment. Interestingly, **NIMCs** with longer alkyl spacers, **NIMC8** and **NIMC10**, exhibit dual organelle localization in lysosomes and the endoplasmic reticulum (ER) wherein the localization shifts more towards the ER with increasing alkyl spacer length. The photostability of all synthesized **NIMCs** was assessed, and the results display excellent photostability, well suited for long-term imaging application. Consequently, **NIMC6** was selected and applied for determining lysosomal micro-polarity in various cell lines through live-cell imaging. Additionally, the micro-polarity of the ER was also estimated using **NIMC10.** Finally, the potential of **NIMC6** encouraged us to employ it for 3-D spheroid imaging and *in vivo* imaging in *C. elegans*.

Results and discussion

Probe design, synthesis, and characterization

The design strategy of **NIMCs** lies in the suppression of PET to avoid the quenching of fluorescence.[52] Here, we followed a reporter–spacer–targeting (R–S–T) strategy and synthesized a library of eight fluorescent molecules namely NIMC*n* (n = 2–6, 8, 10) by choosing 1,8-naphthalimide as a fluorescent reporter and morpholine as the lysosome targeting unit. The aforementioned units are connected *via* flexible alkyl spacers of varying lengths through a secondary amine at the *peri*-position of the naphthalimide core (Scheme 1). It is well-known that upon increasing the pH of the medium, PET is facilitated from donor morpholine (D) to electron acceptor 1,8-naphthalimide (A), leading to fluorescence quenching.[53] To overcome this quenching and to develop a pH-tolerant fluoroprobe we modulated the distance between the D–A pair by introducing a flexible alkyl spacer of increasing length from two to ten carbons. Such an elongation of the distance between the D–A pair causes a reduction in the extent of electron transfer. A distance greater than 0.7 nm, similar to the alkyl spacer length of six-carbon chains, is known to drastically reduce the electron transfer rate between the D–A pair.[54] Such a suppression in electron transfer rate results in an unaltered fluorescence intensity throughout the pH scale. Additionally, the lone pair on the nitrogen atom of the secondary amine participates in intramolecular charge transfer (ICT) with the 1,8-naphthalimide core making **NIMCs** excellent non-flexible ICT probes.[55] Such an ICT character introduces an efficient solvatochromism in **NIMCs**, making them potent probes for determining organelle micro-polarity.

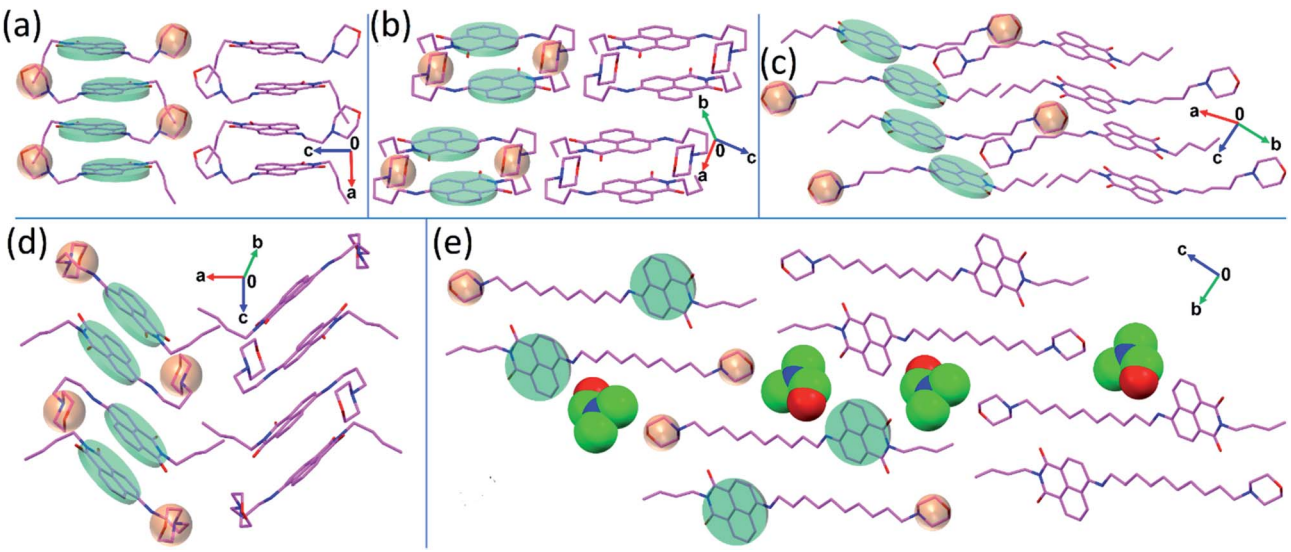

Fig. 1 Representation of the solid-state geometry of the synthesized NIMCs, (a) NIMC2, (b) NIMC3, (c) NIMC5, (d) NIMC4 and (e) NIMC10 obtained from the single-crystal X-ray diffraction. Crystal packing reveals that the molecules are stacked *via* π···π interactions and the shorter alkyl spacers adopt a bent chain conformation, while a straight chain geometry is adopted by intermediate and longer alkyl spacers.

Taking into account the above design strategy, we synthesized **NIMC2–6**, **8**, and **10**, according to Scheme 1. The detailed synthetic procedure of **NIMCs** is provided in the ESI.† In brief, **NIMCs** were obtained by substituting the bromine atoms of 4-bromo-1,8-naphthalimide with *n*-morpholinoalkane-1-amines. Wherein, *n*-morpholinoalkane-1-amines were synthesized by substituting one bromine of 1,*n*-dibromoalkanes with phthalimide followed by the substitution of other bromine atoms with morpholine and finally deprotecting the phthalimide moiety using $N_2H_4 \cdot H_2O$.

After the synthesis, **NIMCs** were characterized by ^{1}H, ^{13}C-NMR spectroscopy and mass spectrometry. Single crystals of **NIMC2**, **NIMC3**, **NIMC4**, **NIMC5**, and **NIMC10** were grown by solvent evaporation of suitable solvent mixtures (see the ESI† for details) for several days and were characterized by single-crystal X-ray diffraction analysis. The details of the entire crystallographic data are tabulated in Table S8.† Crystal structure analysis reveals that **NIMC2** crystallizes in the orthorhombic *Pbca* space group, with constituent molecules being stacked along the crystallographic *a* axis *via* π···π interactions between naphthalene monoimide rings. The short length of the alkyl spacer in **NIMC2** allows the morpholine moiety to be in close proximity to the aromatic core (Fig. 1a). **NIMC3** crystallizes in the orthorhombic *Pbcn* space group, with constituent molecules stacked in a herringbone fashion, where the alkyl spacer bends to a greater extent, allowing the morpholine moiety to come closer to the aromatic core (Fig. 1b). **NIMC4** crystallizes in the triclinic $P\bar{1}$ space group and structural analysis confirms the molecular assembly through alternate π···π and C–H···π interactions along the *a* axis. Interestingly, in this case, the alkyl spacer has been found to bend significantly, mimicking a scorpion tail-like conformation that brings the morpholine moiety in very close proximity to the aromatic core (Fig. 1d). **NIMC5** crystallizes in the triclinic $P\bar{1}$ space group and the constituent molecular layers are assembled *via* π···π interactions between the aromatic cores along the *b* axis (Fig. 1c). In this case, the alkyl spacer has been found to adopt a straight-chain conformation, perhaps to favor hydrophobic interactions for attaining greater thermodynamic stability.[56] Furthermore, **NIMC10** crystallizes in the triclinic $P\bar{1}$ space group, with constituent molecules being uniformly stacked *via* π···π interactions along the *a* axis. Here also the alkyl spacer embraces a straight-chain conformation very similar to that of **NIMC5**, to promote hydrophobic interactions. Hence, structural analysis elucidates the stark difference in the structure of **NIMCs**, where the shorter alkyl spacer adopts a bent chain conformation bringing the

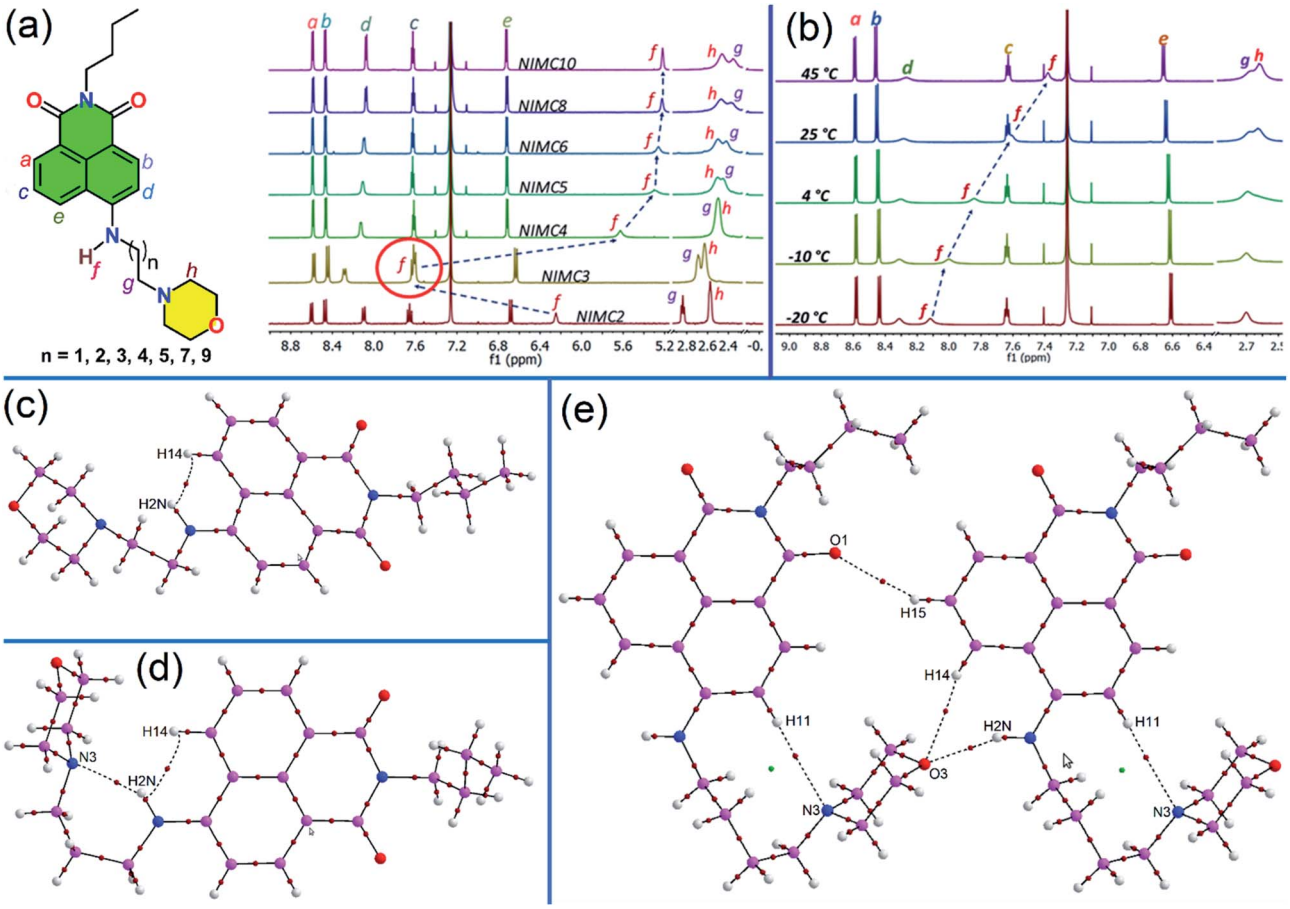

Fig. 2 (a) Comparative ^{1}H-NMR spectra of all **NIMCs** in $CDCl_3$ at RT, and an unexpected downfield shift of the secondary amine proton in **NIMC3** was observed which prompted us to carry out (b) a variable temperature-dependent NMR in $CDCl_3$. QTAIM analysis of (c) **NIMC2**, (d) **NIMC3**, and (e) **NIMC4**, respectively. The bond critical points are shown as brown spheres and ring critical points as green spheres.

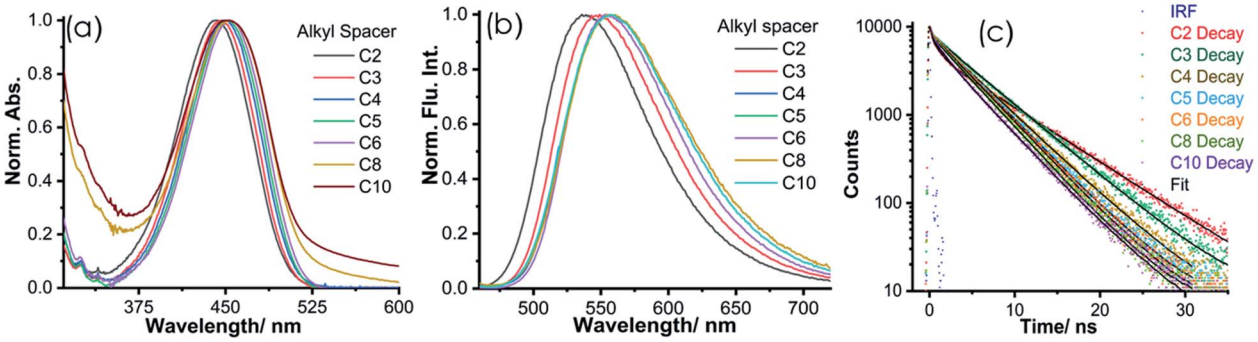

Fig. 3 Representation of photophysical properties: (a) absorption, (b) emission (λ_{ex} = 450 nm), and (c) emission lifetime of the synthesized NIMCs in water (pH = 6.0), where the fluorescence decays were recorded using a 440 nm excitation LASER.

morpholine moiety in close proximity to the NI core. In contrast, intermediate and long alkyl spacers direct the morpholine moiety far away from the NI core. Fascinatingly, the crystal structure of **NIMC10** reveals that the long alkyl spacer enables the morpholine moiety of the other molecule to be in the adjacency of neighboring naphthalimide (Fig. 1e).

With the aim of understanding the behavior of **NIMCs** in solution, a comparative ^{1}H-NMR of all the synthesized **NIMCs** was performed in $CDCl_3$ at room temperature (RT), where the comparative proton NMR plot displays an unexpected downfield shift ($\delta = 7.62$) of the secondary amine proton in the case of **NIMC3** (Fig. 2a). The systematic comparison of chemical shifts (δ) reveals that the introduction of different alkyl spacers does not produce any significant shift of the aromatic protons in **NIMCs** (Fig. 2a). However, the downfield shift for **NIMC3** might be attributed to the formation of intramolecular hydrogen bonding between the secondary amine proton (N2H) and the nitrogen lone pair of the morpholine moiety. To obtain further insight, we also performed a variable temperature ^{1}H-NMR experiment for **NIMC2**, **C3**, and **C4** (Fig. 2b, S2 and S3†), in $CDCl_3$. Eventually, we found a gradual upfield shift of the amine proton of **NIMC3** with increasing temperature, whereas the other congeners display a considerably less shift (Fig. 2b, S2 and S3†), also signifying the formation of intramolecular H-bonding in the case of **NIMC3**. To comprehend such H-bonding and other non-covalent interactions present, we carried out an analysis of the topological parameters (Table S10†) for a few selected motifs highlighting the involvement of N–H hydrogen bond donors in **NIMC2** (Fig. 2c), **NIMC3** (Fig. 2d) and **NIMC4** (Fig. 2e) using QTAIM.[57–59] Interestingly, it has been observed that the molecular conformation of **NIMC3** shows the existence of a stable six-membered ring, formed *via* an intramolecular N–H···N hydrogen bond (involving H2N and N3), corroborated by the presence of a bond path and a bond critical point (BCP) (3, −1) (shown by the brown colored circle in Fig. 2d). The formation of such a six-membered ring through the directional N–H···N (H-bond) interaction makes the secondary amine proton of **NIMC3** highly deshielded and hence exhibits the maximum downfield shift.[60] Similarly in the case of **NIMC2**, Fig. 2c shows that intramolecular N–H···H–C interaction (involving H2N and H14) locks the molecular conformation resulting in a relatively reduced magnitude of the downfield shift. The presence of intermolecular N–H···O and the absence of intramolecular N–H···N interactions (Fig. 2e and S1†) in higher analogs due to the straight chain conformation adopted by the alkyl spacer contribute to almost similar shifts of secondary amine protons as observed in the NMR spectra (Fig. 2a).

Photophysical investigation of NIMCs

To obtain a deeper insight into the photophysical properties of **NIMCs**, we recorded their absorption and emission spectra, as well as fluorescence lifetime decays in an aqueous medium at pH 6.0. The absorption and emission profiles of **NIMCs** reveal that their absorption maximum lies at around 450 nm whereas

Table 1 Photophysical parameters of all NIMCs in an aqueous medium (pH = 6)

Probes	λ_{max}^{abs}/nm	ε^a/M^1 cm^{-1}	λ_{max}^{em}/nm	$\Phi_F{}^b$	Brightness ($\Phi_F \times \varepsilon$)/M^{-1} cm^{-1}	$\tau_{avg}{}^c$/ns
NIMC2	441	16 000	538	0.22	3520	6.9
NIMC3	446	10 800	548	0.47	5076	5.4
NIMC4	449	12 000	554	0.34	4080	4.6
NIMC5	452	11 600	553	0.27	3132	4.3
NIMC6	454	12 200	556	0.32	3904	4.2
NIMC8	453	11 000	559	0.23	2530	4.1
NIMC10	452	11 400	558	0.08	912	4.2

[a] ε is the molar extinction coefficient. [b] Φ is the fluorescence quantum yield, calculated with respect to fluorescein in 0.1 N NaOH.[61] [c] τ is the average fluorescence lifetime.

their emissions fall in the range of 490–720 nm (Fig. 3a and b) (photophysical values are tabulated in Table 1). **NIMC2** shows absorption and emission maxima centered at 441 nm and 538 nm, whereas the absorption and emission maxima are shifted to 454 nm, 452 nm, and 556 nm, 559 nm for **NIMC6** and **NIMC10**, respectively (Fig. 3a and b). A comparative analysis of the spectral behavior indicates that **NIMCs** with intermediate and longer alkyl spacers exhibit almost similar absorption and emission maxima, where **NIMC2** and **C3** show a significant hypsochromic shift in absorption and emission maxima compared to their higher congeners. This hypsochromic shift most possibly could be attributed to the hydrogen bonding interaction between the lone pair of the secondary amine nitrogen and the protonated morpholine hydrogen at pH 6 (Fig. S4†).

Further, the comparative absorption spectra also indicate a significant tailing effect in absorption at a higher wavelength in the case of **NIMC8** and **C10** (Fig. 3a) which perhaps arises due to lower solubility of the long alkyl chains in water. The fluorescence quantum yield of the synthesized **NIMCs** in the aqueous medium (pH = 6) was also determined using fluorescein as a reference.[61] **NIMCs** show fluorescence quantum yields ranging from 0.47–0.08 and the average fluorescence lifetime ranges from 6.9–4.2 ns, which is quite desirable for live-cell fluorescence imaging and fluorescence lifetime imaging microscopy (FLIM) (Fig. 3c and Table 1). The fluorescence lifetimes were also found to decrease gradually with increasing alkyl spacer length which might arise from the self-assembling effect in the case of higher congeners. The outcome of all spectroscopic measurements of **NIMCs** established that they are visible light excitable with a large Stokes shift, along with high fluorescence quantum yield and brightness, evincing their suitability towards fluorescence-based imaging applications.

Fluorescence intensity variation with the pH of the medium

To elucidate the applicability of **NIMCs** towards imaging lysosomal activity, we inspected their emission behavior with the variation of pH to screen their pH tolerance. Hence, we recorded the emission spectra of all **NIMCs** at pH 2.50 ($NIMCH^+$) and 9.25 (**NIMC**), by exciting at 450 nm (Fig. 4a and S9†). The emission profiles indicate a decrease in fluorescence intensity with a small bathochromic shift in the emission maximum with increasing alkyl spacer length at both the pH values (Fig. 4a and S9†). Additionally, we plotted the difference in fluorescence intensities ΔFlu. Int. = $Int._{(NIMH^+)} - Int._{(NIM)}$ at λ_{max}^{em} against the alkyl spacer length for all **NIMCs** (Fig. 4b). The plot indicates a gradual decrease in ΔFlu. Int. with increasing alkyl spacer length from C2 to C6. Interestingly, the difference starts increasing again with increasing alkyl spacer length from C8 to C10 showing a minimal effect in the case of C6 (Fig. 4b). Further, we examined the variation of fluorescence intensity not only at highly acidic or basic regions but also for the whole range of pH. The fluorescence titration with pH showed

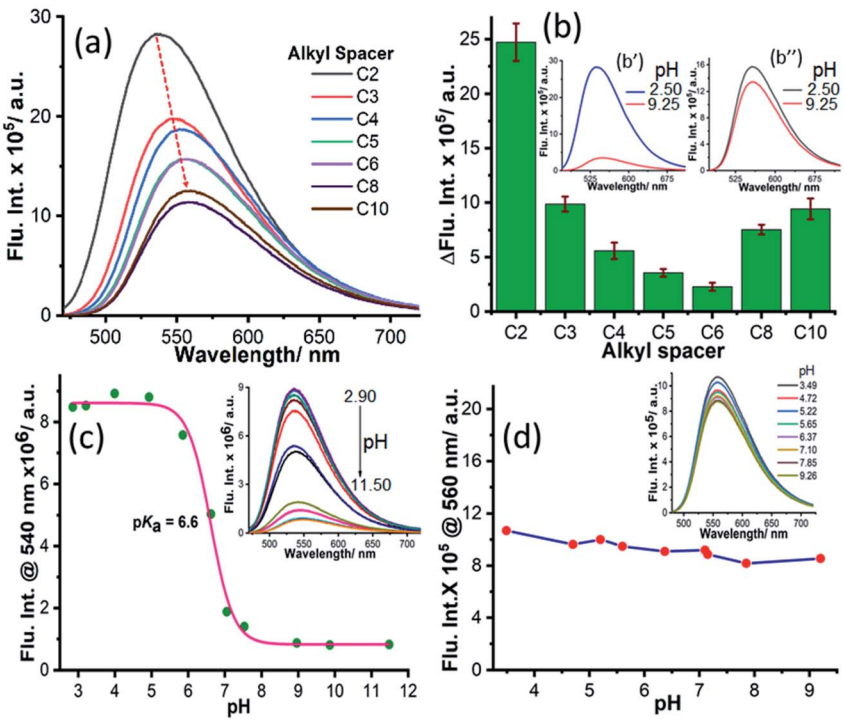

Fig. 4 The pH-dependency of the emission profile of NIMCs, where (a) presents the emission profiles of all NIMCs at pH 2.5 and (b) presents the difference in fluorescence intensity (ΔFlu. Int.) at the emission maxima of individual NIMCs between pH 2.5 and 9.2, plotted against alkyl spacer length of the alkyl spacer where the inset (b′ and b″) presents the change in the emission profiles of NIMC2 and NIMC6 at these two pH values. The variation of fluorescence intensity at 540 nm and 560 nm is plotted against pH for NIMC2 and NIMC6, respectively (c and d), and the corresponding inset shows the change in the emission profiles.

a quenching of fluorescence intensity with increasing pH where the obtained values yield a sigmoidal fitting with a pK_a around 6.8 to 5.0 for **NIMCs** except for **NIMC6**, which exhibits a negligible variation of fluorescence intensity with pH (Fig. 4c, d and S10–S13†) in the selected pH window. The inverse relationship of fluorescence intensity with pH is attributed to the well-known phenomenon of photo-induced electron transfer (PET) from the lone-pair of morpholine nitrogen (D) to the electron-deficient naphthylamide ring (A).[62] The straight-chain conformation adopted by the alkyl spacers of **NIMC5** and **NIMC6** places the D–A units of constituent molecules far away from each other causing the suppression in intramolecular PET, and as a result, they enjoy a minimal change in fluorescence intensities (Fig. 4d and 1c). However, the long alkyl spacers in **NIMC8** and **C10** help the D–A units of neighboring molecules to come in close proximity to each other, facilitating intermolecular PET and hence higher ΔFlu. Int. (Fig. 1e, 4b, and S13†). The short distance between the D–A pair in **NIMC2**, along with the absence of any inter or intramolecular interactions involving morpholine as the donor (Fig. 1a and 2c), makes PET a very facile process, affording the highest ΔFlu. Int. (Fig. 4b and c).[52] However, the presence of intramolecular N–H···N and C–H···N interactions in **NIMC3** (Fig. 2d) and **NIMC4** (Fig. 2e), respectively, confirmed by the presence of bond paths and BCPs (details of interactions shown in Table S10†) reduces their intramolecular PET, leading to lower values of ΔFlu. Int. than those of **NIMC2** (Fig. 4b). Therefore, **NIMC6** emerges as a potent pH-tolerant fluorescent probe for lysosomal imaging.

Polarity-dependent photophysics

Specifically, the selected pH-invariant fluorophore **NIMC6** and other synthesized **NIMCs** were subjected to the measurement of absorption, emission, and fluorescence lifetimes (using time-correlated single-photon counting) in solvents of varying polarity, to validate their applicability for probing lysosomal micro-polarity. **NIMC6** is pH invariant, and hence, to get further insight we checked its optical purity in water (pH 6.0). A suitable overlap between the absorption and excitation spectra was observed, validating its optical purity and its suitability towards live-cell imaging (Fig. S5e†). Further, the optical purity of all other **NIMCs** in water was also checked where the absorption and excitation spectra of **NIMC2** and **C3** show slight deviation, which might be due to hydrogen bonding interaction between the protonated morpholine and the lone pair of the secondary amine nitrogen at that pH (Fig. S5 and S4†). **NIMCs** contain a secondary amine group at the *peri*-position of the 1,8-naphthalimide ring and the nitrogen lone-pair is capable of conjugating with the imide group through the naphthalene π-conjugated ring. Fluorescent molecules containing both electron-donating and accepting groups connected *via*

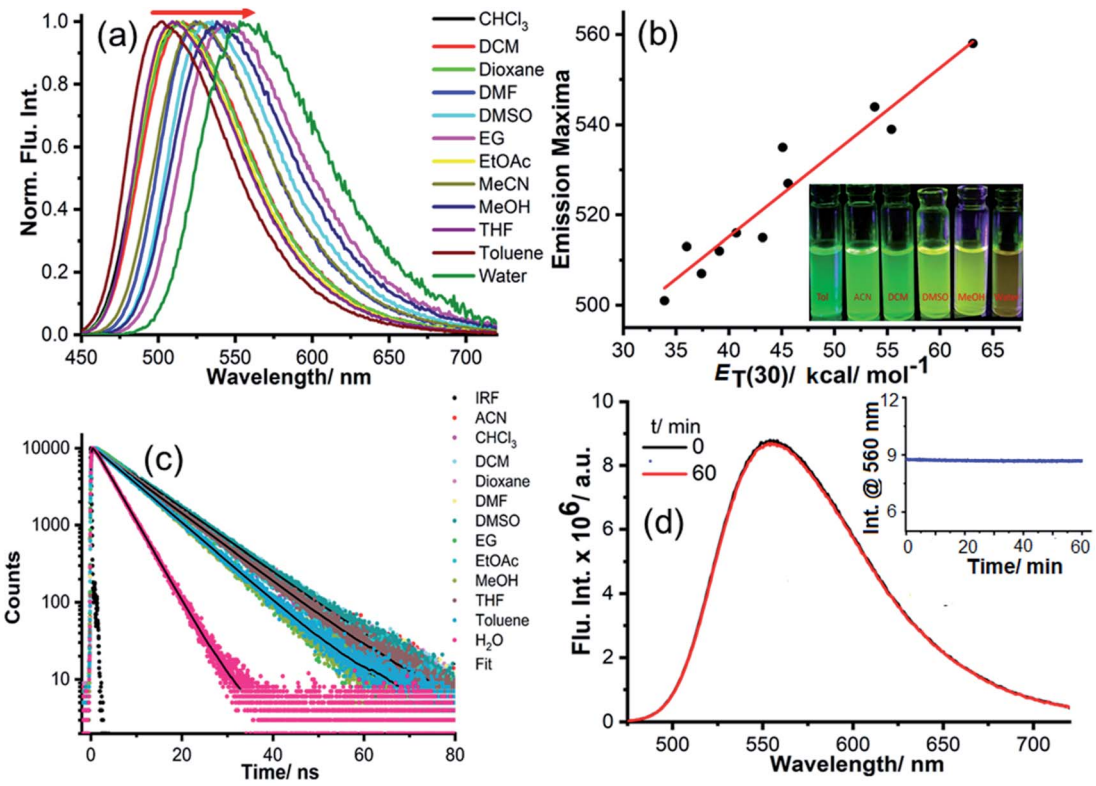

Fig. 5 Solvent-dependent emission properties of NIMC6. (a) Bathochromic shift of emission maxima with increasing solvent polarity. (b) Emission maximum varies linearly ($R^2 = 0.93$) with the solvent polarity scale $E_T(30)$, and the inset shows its ICT character further confirmed by the visible color change. (c) Solvent-dependent fluorescence lifetimes of NIMC6 in various solvents. (d) Photostability of NIMC6, where the fluorescence intensity remains unaltered under continuous illumination with 450 nm light and the inset shows the corresponding fluorescence kinetics.

a conjugated π-linker are known as intramolecular charge transfer (ICT) dyes, and possess a high dipole moment in the ground and in the excited state.[63,64] The photophysical investigations indicate that all **NIMCs** exhibit typical characteristics of ICT dyes because they show a small red shift in absorption maxima and a huge bathochromic shift in emission maxima with increasing solvent polarity (Fig. 5a, S6 and S7, for values see Tables S1–S7†). Eventually, the absorption and emission maxima of **NIMC6** in toluene are 426 nm and 502 nm, respectively, but in a highly polar aqueous medium, they shift to 453 nm and 556 nm (Fig. 5a and Table S5†). This larger Stokes shift of ICT probes in various dielectric media can be rationalized by the Lippert–Mataga equation as follows:

$$\Delta\nu = \frac{2\Delta f}{hca^3}\left(\overrightarrow{\mu_e} - \overrightarrow{\mu_g}\right)^2 + b,\quad \Delta f = \left(\frac{\varepsilon - 1}{2\varepsilon + 1} - \frac{n^2 - 1}{2n^2 + 1}\right)$$

where $\Delta\nu = \nu_{abs} - \nu_{em}$ stands for the Stokes shift, ν_{abs} and ν_{em} are absorption and emission frequencies, respectively, in cm^{-1}, h is the Planck's constant, c is the velocity of light in a vacuum, a is the Onsager radius and b is a constant. Δf is the orientation polarizability, ε is the dielectric constant of the medium, n is the refractive index, and $\overrightarrow{\mu_e}$ and $\overrightarrow{\mu_g}$ are the dipole moments of the emissive and ground states, respectively. $(\overrightarrow{\mu_e} - \overrightarrow{\mu_g})^2$ is proportional to the slope of the Lippert–Mataga plot.[65] From this equation, it can be inferred that the emission maximum varies linearly with the solvent polarity scale $E_T(30)$, as observed for **NIMC6** and other analogs (Fig. 5b and S7†).

Such linear polarity-dependent emission properties with a large Stokes shift corroborate a non-twistable ICT character for **NIMCs**. To acquire further knowledge of their photophysical properties, we recorded the fluorescence lifetime decay in different solvents which exhibits single-exponential decay (Fig. 5c). The excited-state lifetime of **NIMCs** increases with increasing solvent polarity, signifying their applicability in fluorescence lifetime imaging. In a nutshell, polarity-dependent measurement confirms their applicability for determining lysosomal micro-polarity.

Photostability of NIMC6

The photobleaching effect is a well-known phenomenon in fluorescence quenching which imposes limitations on their utility in fluorescence-based live-cell imaging. Several fluoroprobes get photo-bleached due to their low photostability when excited using high LASER power in confocal microscopy. Hence, these probes are less suitable for prolonged imaging purposes. To test their applicability for long-term imaging, the photostability of **NIMC6** was measured by exciting with 450 nm light (450 W xenon lamp, 100 lx) and the fluorescence kinetics was monitored for an hour (Fig. 5d). No change in fluorescence intensity was observed in the experimental time frame indicating its high photostability. Additionally, the photostability of **NIMC6** was also compared with that of commercially available LysoTracker Green by exciting both with 480 nm light. The result displays similar photo-stability of **NIMC6** to LysoTracker Green further evidencing its potential towards long-term lysosomal imaging (Fig. S14†). The photostability of **NIMC6** and LysoTracker Red was compared under live-cell imaging conditions using confocal laser excitation (Fig. S15†), *vide infra,* which establishes its prospects as a long-term live-cell imaging agent.

Live-cell imaging

Sub-cellular localization. Following the detailed spectroscopic investigations, live-cell imaging experiments were

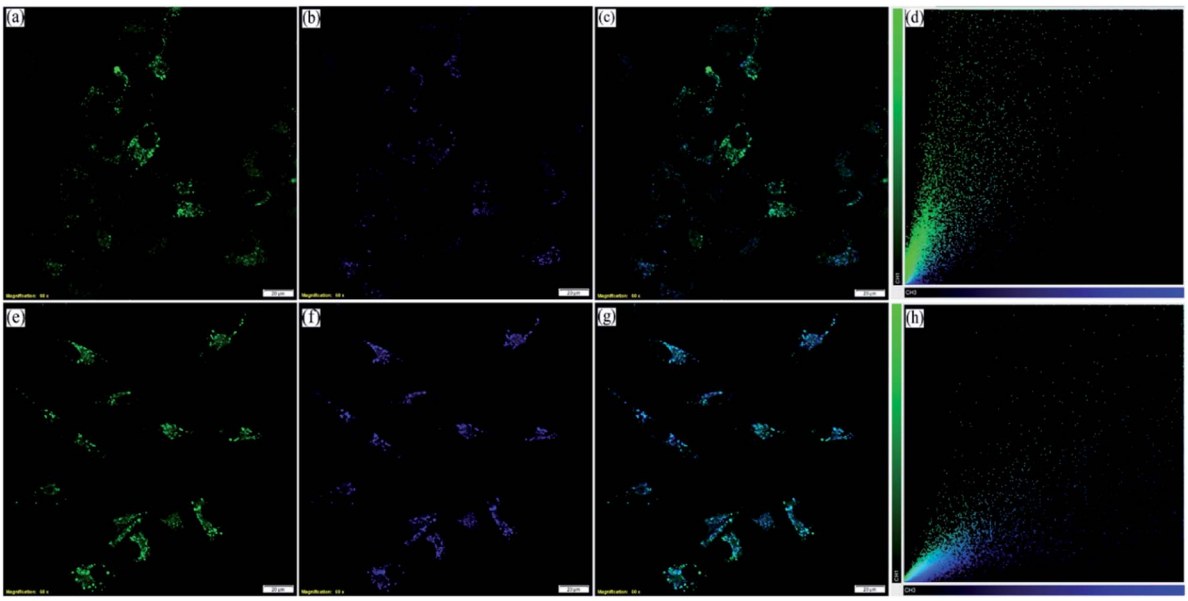

Fig. 6 CLSM images of BHK-21 cells stained with (a) 0.2 μM **NIMC2** and (b) 0.3 μM LysoTracker Deep Red; (c) merged image of (a) and (b); (d) scatter plot showing Pearson's correlation coefficient of 0.89 ± 0.04; (e) 0.2 μM **NIMC6**; (f) 0.3 μM LysoTracker Deep Red; (g) merged image of (e) and (f); (h) scatter plot showing Pearson's correlation coefficient of 0.88 ± 0.02 (scale bar: 20 μm) [$\lambda_{ex}/\lambda_{em}$ = 488 nm/500–540 nm, $\lambda_{ex}/\lambda_{em}$ = 640 nm/650–680 nm, dwell time: 8 μs per pixel, 1 airy disk, laser power: 0.2%].

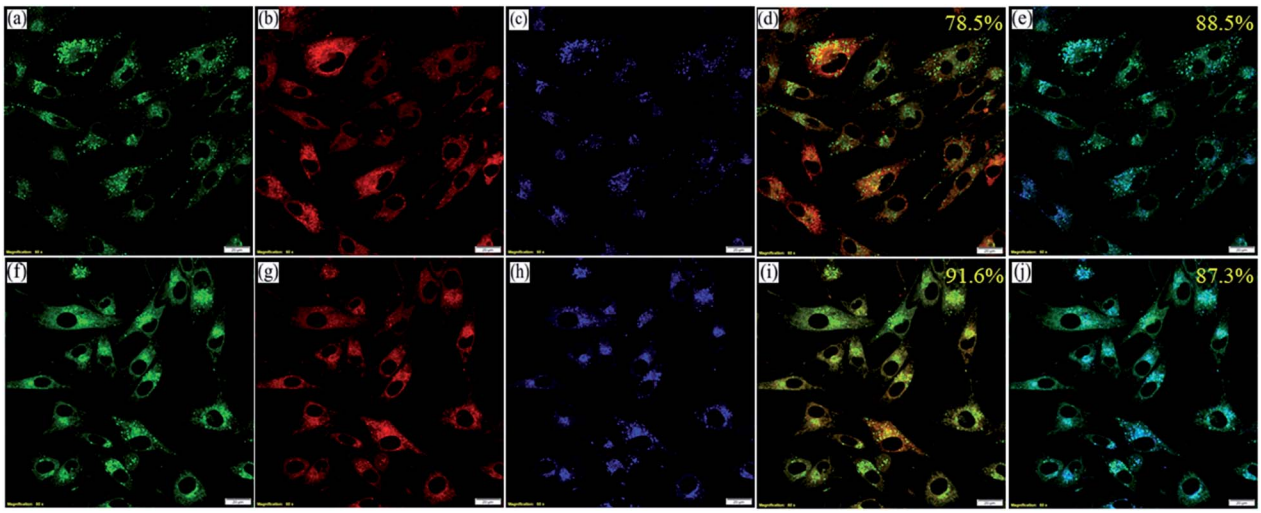

Fig. 7 CLSM images of BHK-21 cells stained with (a) 0.2 μM **NIMC8**, (b) 0.3 μM ER Tracker Red, and (c) 0.3 μM LysoTracker Deep Red; (d) merged image (Pearson's correlation coefficient of 0.78 ± 0.03) of (a) and (b); (e) merged image (Pearson's correlation coefficient of 0.88 ± 0.02) of (a) and (c); staining with (f) 0.2 μM **NIMC10**, (g) 0.3 μM ER Tracker Red, and (h) 0.3 μM LysoTracker Deep Red; (i) merged image (Pearson's correlation coefficient of 0.91 ± 0.02) of (f) and (g); (j) merged image (Pearson's correlation coefficient of 0.87 ± 0.04) of (f) and (h) (scale bar: 20 μm) [$\lambda_{ex}/\lambda_{em}$ = 488 nm/500–540 nm, $\lambda_{ex}/\lambda_{em}$ = 561 nm/575–620, $\lambda_{ex}/\lambda_{em}$ = 640 nm/650–680 nm, dwell time: 8 μs per pixel, 1 airy disk, laser power: 0.2%].

performed to visualize the intracellular localization of the **NIMCs**. Prior to performing extensive live-cell microscopy, we first monitored the cytotoxic effects of all **NIMCs** by the standard MTT [3-(4,5-dimethylthiazole-2-yl)-2,5-diphenyltetrazolium bromide] assay in normal BHK-21 (baby hamster kidney) cell lines. Following a 24 h incubation of BHK-21 cells, cytotoxicity assays were performed and the results indicated that the half-maximal inhibitory concentrations, *i.e.*, IC_{50} values, range from 5 μM to 10 μM for **NIMCs** (Fig. S16†). Hence, considering this inhibitory concentration range, we used 0.2 μM probe, as ~90% of cells were viable in each case, to execute live-cell fluorescence imaging. Furthermore, cellular uptake phenomena of **NIMCs** were studied to understand their internalization process through the plasma membrane. At two different incubation temperatures, 4 °C and 37 °C, comparable fluorescence signals were observed from the lysosomal compartments suggesting a pH-driven simple diffusion mechanism for the internalization process. To optimize the incubation time of the **NIMCs**, the cells were incubated for different periods. Much to our delight, it was observed that a 10 min incubation period is sufficient for confocal imaging, indicating fast and efficient internalization of **NIMCs**. Besides, to confirm the colocalization of the synthesized **NIMCs** inside the lysosomal compartments, BHK-21 cells were stained with all the **NIMCs** at 0.2 μM concentration along with 0.3 μM commercially available LysoTracker Deep Red for 10 min. Upon excitation with 488 nm and 640 nm laser, fluorescence signals coming from the cells were collected, from which the shapes of lysosomes were deciphered with low background confirming their suitability for lysosomal imaging. Further, sequential imaging was performed to compute the colocalization inside the lysosomal compartment, which revealed high Pearson's coefficients around 0.9 (Fig. 6, and see the ESI† for others), indicating an efficient localization of all the **NIMCs** in the lysosomal compartment.

However, to confirm the accumulation of **NIMCs** exclusively in the lysosomes, they were co-stained with two other commercially available organelle-specific dyes, namely

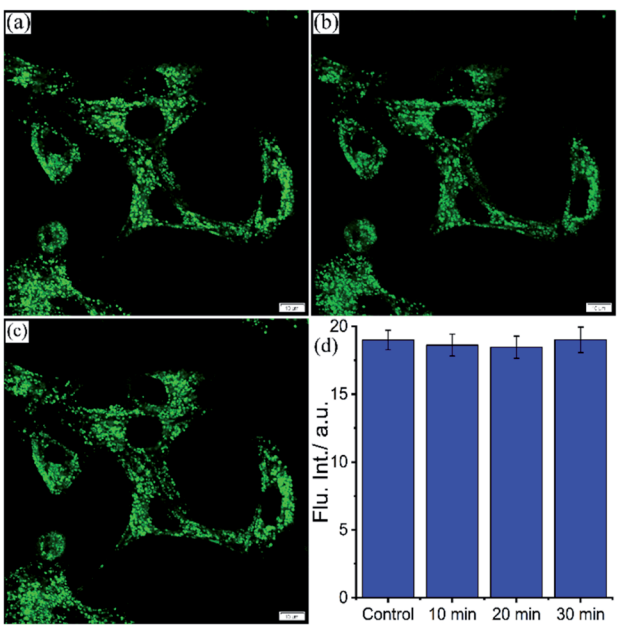

Fig. 8 CLSM images of BHK-21 cells stained with (a) 0.2 μM **NIMC6** and stimulated with 20 μM chloroquine for (b) 10 min and (c) 30 min; (d) the average fluorescence intensity measured in different ROIs from the same field of view (FOV) at the aforementioned time-points of the experiment (see the ESI† for complete information) (scale bar: 10 μm) [λ_{ex} = 488 nm, λ_{em} = 500–540 nm, dwell time: 8 μs per pixel, 1 airy disk, laser power: 0.2%].

MitoTracker Red FM and ER-Tracker Red. The colocalization analysis divulged that signals from the **NIM** (C_2–C_6) lightened up only the lysosomal compartments with bright green fluorescence (Fig. 6, S17 and S18†), whereas the colocalization studies for **NIMC8** and **NIMC10** provided an intriguing result. In this case, fluorescent signals were observed from both lysosomes and the endoplasmic reticulum (ER), which was further verified through colocalization studies by co-incubation with **NIMC8** or **NIMC10**, ER-Tracker Red, and LysoTracker Deep Red, and through sequential imaging (Fig. 7). Possibly, the longer alkyl chain of **NIMC8** and **NIMC10** accounted for greater hydrophobicity, driving them to localize in the ER. As the endoplasmic reticulum (ER) is a major site for lipid synthesis and metabolism, it poses a hydrophobic environment, which induces a hydrophobicity driven accumulation inside the ER of these two derivatives. Therefore, dual organelle localization was achieved by **NIMC8** and **NIMC10**. Notably, the result implies that a long alkyl spacer plays a decisive role even if a pH-directive moiety is present for localization in the lysosomes. Besides, our observation creates another opportunity to get more insights into ER–lysosome contact through this dual-mode targeting. Therefore, pH-dependent spectroscopic measurements and live-cell imaging indicate that **NIMC6** is a superior choice among other congeners for imaging lysosomal activity.

Effect of stimulated pH change in live cells

Lysosomes are acidic organelles crucial for the digestion of proteins, lipids, and enzymes and thereby maintain cellular homeostasis.[66] Lysosomal pH is subject to change during autophagy due to the accumulation of undigested and insoluble metabolites.[67,68] pH-independent lysosome targeting probes hold a prominent place due to their efficient localization and unaltered emission signal even if lysosomal pH varies. Chloroquine causes lysosomal stress by inducing lysosomal proton leakage resulting in a gradual increase of lysosomal pH.[26,69] Here, the effect of lysosomal pH variation on the emission intensity of **NIMC6**, in the presence of lysosomal stressor chloroquine, is delved into. For this purpose, live BHK-21 cells were co-incubated with 20 μM chloroquine and 0.2 μM **NIMC6** for 10, 20, and 30 min. The average fluorescence intensity was measured over different ROIs in both same field of view (FOV) and different FOVs of the stimulated and untreated cells at different time points (Fig. 8a, d, S19a and b†). The fluorescence intensity of **NIMC6** remains invariant for both stimulated and untreated cells throughout the entire period of incubation. Such a fascinating result encouraged us to visualize the lysosomal activity with the aid of pH-tolerant probe **NIMC6**.

Fluorescence recovery after photobleaching (FRAP)

The synthesized **NIMCs** are quite excellent in terms of low cytotoxicity, cell permeability, and brightness. Nonetheless, based on the comprehensive spectroscopic and initial microscopic results, we speculated that **NIMC6** would be superior to other analogs. We verified this apprehension by understanding the binding properties of **NIMCs** in the lysosomal compartments. Fluorescence recovery after photobleaching (FRAP) is a widely used approach that provides information regarding the dynamics of binding interactions, spatial distribution, and diffusibility of a constituent of interest.[70,71] The FRAP experiment is a useful technique to judge the suitability of a probe to image in living cells for a longer period. Hence, we performed the FRAP experiment to explicate the diffusional properties of the synthesized **NIMCs** to acquire further acumen into the local

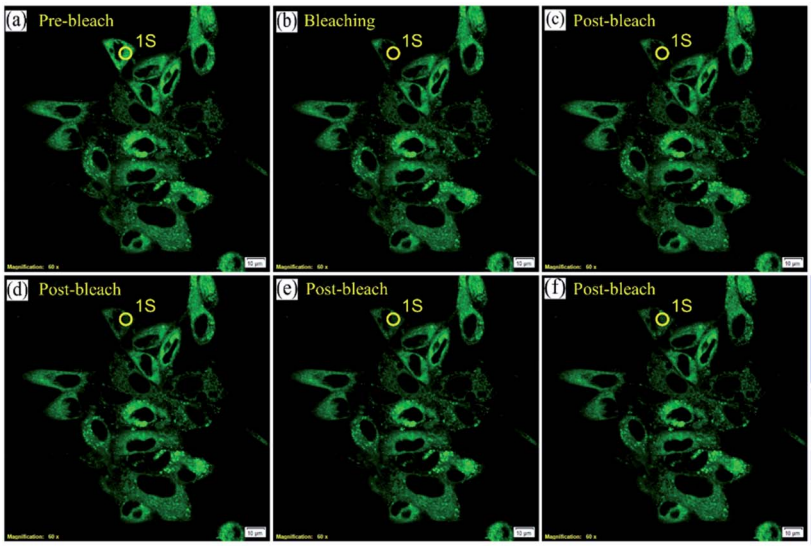

(h)

NIMOR probes	Half time for recovery (s)	Diffusion coefficient ($\mu m^2.s^{-1}$)
C2	16.05	0.009
C4	37.07	0.004
C6	56.98	0.0027
C8	69.83	0.0022
C10	103.19	0.0016

Fig. 9 Fluorescence recovery after photobleaching (FRAP) measurement was performed in the BHK-21 cell line stained with 0.2 μM **NIMC6** probe. The results show the bleaching and post-bleaching (recovery) phenomena. The circular region (1S) represents the bleached region: (a) pre-bleach cycle; (b) bleaching; (c), (d), (e) and (f) show post-bleaching recovery of fluorescence, respectively (scale bar: 10 μm); (g) FRAP recovery kinetics of **NIMC2**, **C4**, **C6**, **C8** and **C10** derivatives. The fluorescence emission was collected from 500 to 550 nm [$\lambda_{ex}/\lambda_{em}$ = 488 nm/500–540 nm, photobleach dwell time: 100 μs per pixel, 1 airy disk, bleaching duration: 5 s, bleaching laser power: 20%].

organization exhibited by them. To perform the FRAP experiment the scanning parameters, *i.e.*, scanning speed, laser power, and bleaching duration, were optimized to avoid consequential fluorescence photobleaching due to repetitive imaging. After optimization, the FRAP experiment was performed and the results showed an increase in half-time for recovery with increasing alkyl spacer length. Interestingly, **NIMC2** and **NIMC10** showed the highest and lowest diffusion rate, respectively, whereas **NIMC6** maintained an intermediate diffusional rate (Fig. 9). The smaller size of **NIMC2** enables it to diffuse and bind rapidly, evident from the fastest half-time of recovery where the diffusion coefficients were calculated by fitting the raw FRAP data using the Soumpasis equation:[72,73]

$$\text{Diffusion coefficient, } D_{r_n} = 0.224\frac{{r_n}^2}{\tau_{1/2}}$$

where r_n is the radius of a uniformly bleached spot and $\tau_{1/2}$ is the half-time for recovery. In this case, the effective bleach radius (r_e) and bleaching spot radius were considered equal because of instantaneous bleaching, small bleaching radius, and small pixel size so that the Gaussian profile can be neglected. The FRAP analysis indicates **NIMC2** to be the preferred one for bioimaging applications compared to all other **NIMCs** due to its faster dynamics and intensity recovery. However, **NIMC2** shows the highest pH-sensitive fluorescence compared to all other analogs making it the least favorite due to dynamic lysosomal pH. Additionally, **NIMC10** shows a fair enough pH sensitivity and dual organelle targeting making it less preferable for imaging lysosomal dynamics. Therefore, these two competing parameters establish **NIMC6** as the superior one for imaging lysosomal properties which is also supported by its intermediate diffusion rate.

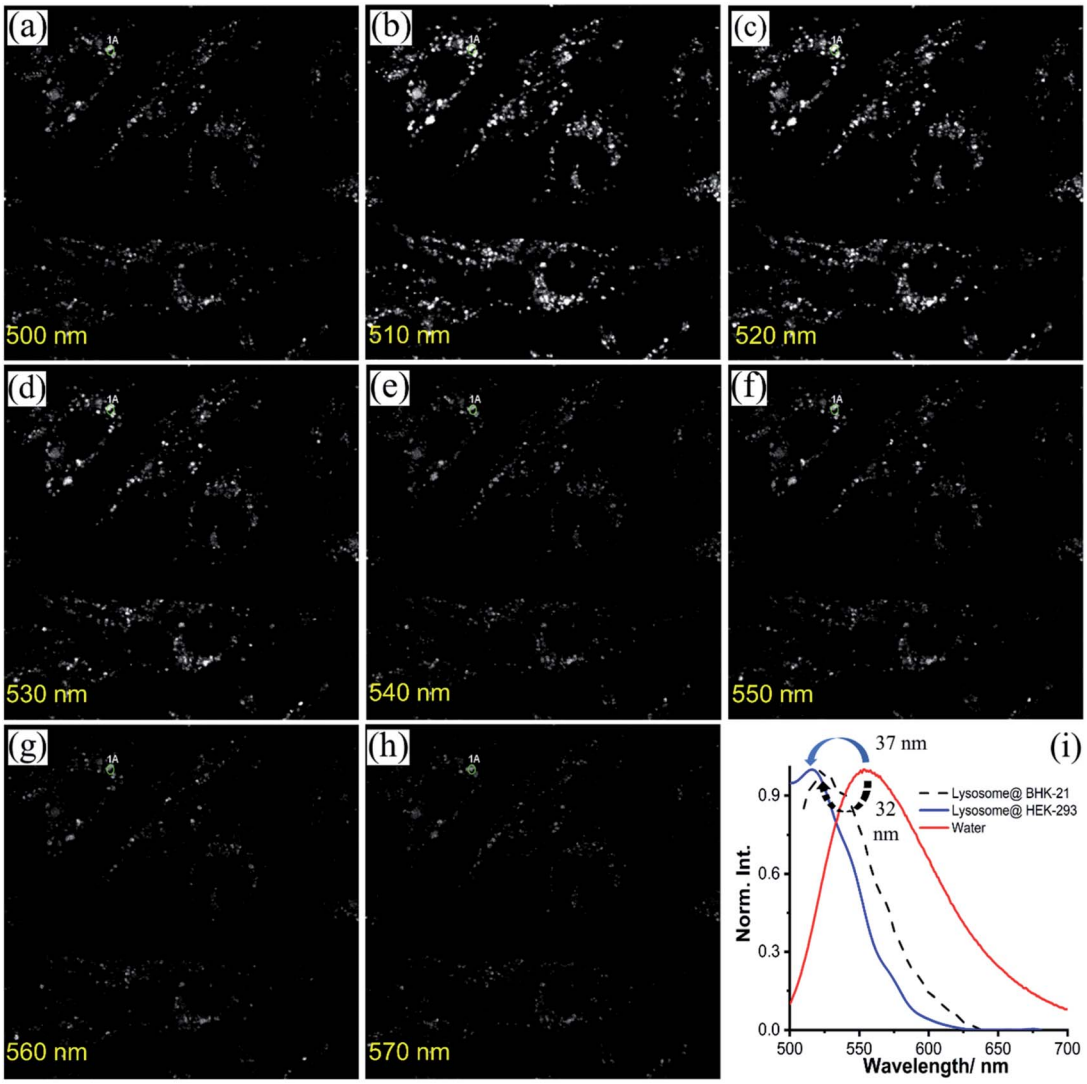

Fig. 10 (a–h) Series of individual images at different wavelengths recorded using the confocal lambda scanning technique; (i) emission spectra of **NIMC6** inside lysosomes (λ_{max} = 524 nm) showing a 32 nm blue shift compared to that of water (λ_{max} = 556 nm). However, the same technique reveals a 37 nm blue shift (λ_{max} = 519 nm) of **NIMC6** inside the lysosomal compartment of HEK-293 cells compared to that of water (i) [λ_{ex} = 488 nm, λ_{em} = 500–700 nm, dwell time: 8 μs per pixel, 1 airy disk, laser power: 1%].

Micro-polarity in live cells

Inspired by the pH-tolerance, lysosomal colocalization, and suitable diffusion rate of **NIMC6**, it is considered as a potential candidate to explore the lysosomal micro-environment in living cells. Lysosomal polarity is an important parameter to monitor as any alteration of such a parameter causes internal environment disorganization under pathological conditions.[33,49,74–76] Hence, monitoring micro-polarity inside the lysosomal compartment by employing the synthesized **NIMC6** would surely be an extra advantage. To perform such measurements, BHK-21 cells were incubated with 0.2 μM **NIMC6** followed by the spectral scanning under a confocal laser scanning microscope. The lysosome rich area gave rise to an emission spectrum having completely different emission maxima of **NIMC6** ($\lambda^{max}_{em(lyso)} = 524$ nm) compared to its emission maxima in bulk water (Fig. 10). Upon comparing the emission maxima, with solvent polarity-dependent emission spectra (Table S5†), surprisingly we found that the micro-environmental polarity in lysosomes was similar to that of acetonitrile in BHK-21 cells. Additionally, we measured the lysosomal micro-polarity in HEK-293 cells by employing the same probe where we found that the micro-polarity was similar to that of dichloromethane (DCM) (Fig. S20 and Table S5†), indicating the potential of **NIMC6** for differentiating the lysosomal micro-environment polarity in various living cells. Further, the accumulation of **NIMC10** inside the endoplasmic reticulum (ER) demonstrates its applicability for monitoring the micro-environment polarity inside the ER. Hence, we performed a spectral scanning experiment to determine ER-micro-polarity by employing **NIMC10** in BHK-21 and HEK-293 cells. **NIMC10** exhibits an emission maximum at around $\lambda^{max}_{em(ER)} = 536$ nm (Fig. S21 and S22†) in both the cell types compared with the solvent polarity dependent emission profile of **NIMC10** (Table S7†), signifying that the micro-environment polarity inside the ER is similar to that of dimethyl sulfoxide (DMSO) for both the cell types. Therefore, the experimental results evidence captivating applicability of **NIMC6** and **NIMC10** towards the determination of lysosomal and endoplasmic reticulum micro-environment polarity in various live cells.

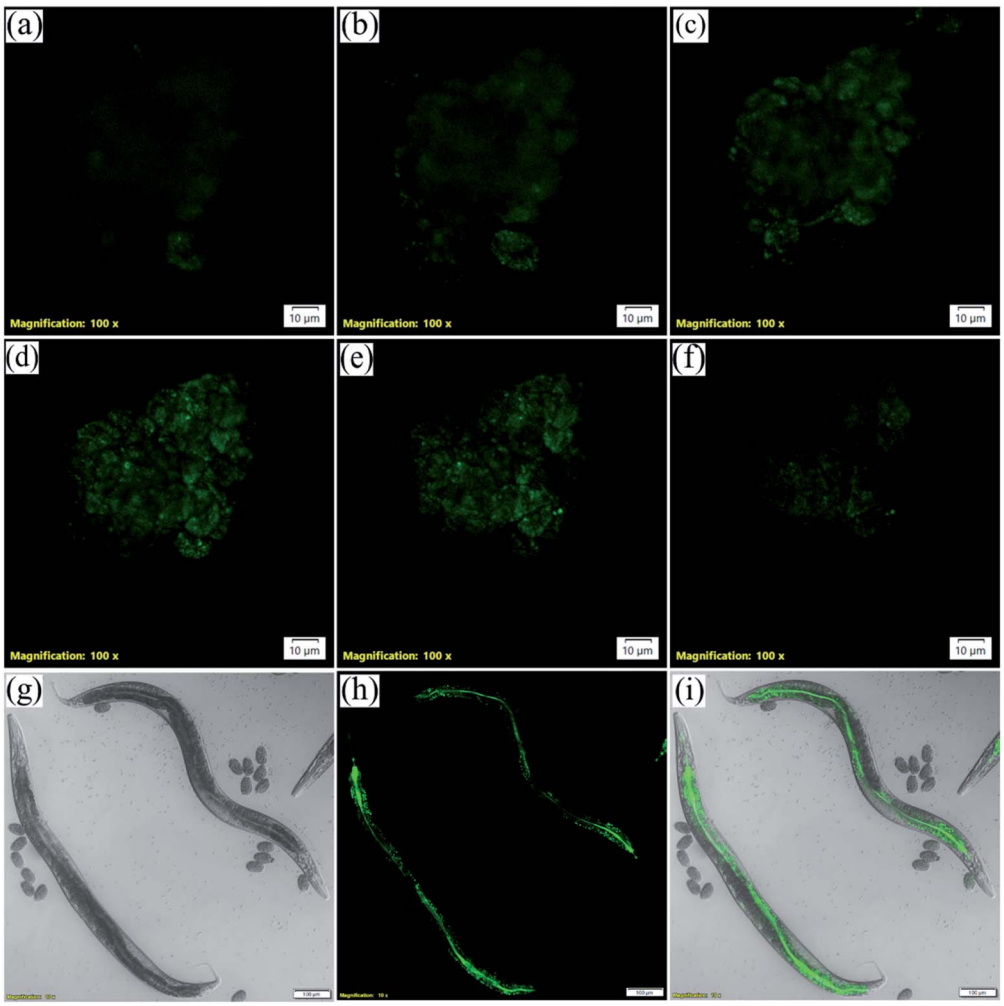

Fig. 11 CLSM images (a–f) of 3D spheroids in different *Z*-planes obtained from BHK-21 and incubated with 0.2 μM **NIMC6** (scale bar 10 μm); images of wild-type N2 worms: (g) bright field, (h) incubated with 5 μM **NIMC6**, (i) merged image showing the *in vivo* distribution of **NIMCs** (scale bar: 100 μm) [$\lambda_{ex} = 488$ nm, $\lambda_{em} = 500–540$ nm, dwell time: 8 μs per pixel, 1 airy disk, laser power: 0.2%].

Imaging of 3D-spheroids and lysosome-related organelles in *C. elegans*

Three-dimensional (3D)-spheroidal cell models have become a mainstay in life science research due to their ability to mimic *in vivo* environments.[77] Cells in monolayer culture lose many of their *in vivo* characteristics. As a result, this platform provides limited predictive value in determining the clinical outcome of the compounds of interest. The use of a technique known as 3D-spheroid culture may be the answer to this conundrum. 3D-cell culture models are better able to reproduce not only the *in vivo* morphology, but also the cell connectivity, polarity, gene expression, and tissue architecture, making them more physiologically relevant and predictive than 2D-models, thereby bridging the gap between *in vitro* and *in vivo* models.[78] As the live-cell microscopy experiments came up with some intriguing results we further wanted to verify the applicability of **NIMC6** in 3D-spheroid imaging. Hence, we cultured spheroids of BHK-21 cells and treated them with **NIMC6** (Fig. 11a–f and S23†). Significant cellular uptake was observed with only 10 min incubation suggesting that the probes possess the potential for imaging in tissue samples.

Caenorhabditis elegans is one of the simplest animal models used for lysosome-related studies.[79] They have gut granules which are acid hydrolase containing membrane-bound cellular compartments often called lysosome-related organelles (LRO).[80,81] These gut granules mostly fill the intestinal cells of *C. elegans*. Hence, to further explore the probe's versatility for bioimaging applications, *C. elegans* were imaged by **NIMC6** staining. The hermaphrodite worms were synchronized and grown to the young adult stage in nematode growth media (NGM) treated with 5 μM **NIMC6** for 60 h at 20 °C. They were transferred to an agar pad on a glass slide and paralyzed with 5 mM levamisole and imaged under a confocal microscope. The intestine and the gut granules are visible as evident from the green channel image (Fig. 11g–i). Therefore, **NIMC6** can be used as a potential marker for staining the LROs in *C. elegans.*

Conclusions

In summary, we have demonstrated an alkyl spacer length variation strategy by simple chemical modification to improve pH-dependent fluorescence quenching and synthesized a series of fluorescent derivatives namely **NIMCs**. Structural analysis reveals that while a shorter alkyl spacer adopts a bent-chain conformation, the intermediate and longer ones adopt a straight-chain conformation. **NIMCs** exhibit similar behavior in the ^{1}H-NMR analysis except **NIMC3** which shows an unexpected downfield shift of the secondary amine proton attributed to the formation of intramolecular H-bonding between the amine proton and the nitrogen lone pair of morpholine. The staining character of most reported PET-lysotrackers is usually driven out of lysosomes and quenched significantly upon the increase in local pH, whereas **NIMC6** retains its fluorescence intensity throughout the pH range. The rationally designed photostable and solvatofluorochromic **NIMCs** showed potential for determining lysosomal micro-polarity under pathological conditions. Further, **NIMC6** is also applicable for specific lysosomal imaging under normal and stress conditions, which is illustrated by colocalization with LysoTracker, Mito-tracker, ER-tracker, and intensity monitoring in the presence of the lysosomal stressor chloroquine. Surprisingly, the higher congeners, *i.e.*, **NIMC8** and **C10**, exhibit dual organelle localization in lysosomes and the endoplasmic reticulum due to augmented lipophilicity. Moreover, specifically selected pH-tolerant **NIMC6** diffuses nicely, with a diffusion coefficient value of 2.7×10^{-3} $\mu m^2\ s^{-1}$, into lysosomes and allows real-time monitoring of lysosome-polarity which is similar to the polarity of acetonitrile. Eventually, the employment of **NIMC6** for 3D-spheroid imaging in BHK-21 cells and *in vivo* imaging in *C. elegans* ascertains its potential as a marker for staining lysosome-related organelles (LRO). Therefore, we strongly believe that pH-tolerant **NIMC6** will emerge as a competent candidate for monitoring lysosome-related dysfunctions and the higher congeners (**NIMC8** & **C10**) play a commendable role in elucidating organelle communication through fluorescence imaging in live cells as well as in animal models.

Data availability

Electronic supplementary information including the synthetic procedure and characterization (^{1}H, ^{13}C-NMR, HRMS) of **NIMCs**, pH and solvent-dependent optical properties, variable temperature ^{1}H-NMR, cell viability of **NIMCs**, live-cell imaging for co-localization analysis, lamda-scanning experiments for micropolarity determination, live-cell 3D spheroid imaging, crystal refinements parameters, inter and intra-molecular interaction table.

Author contributions

SB designed the synthetic procedures and performed the synthesis, characterization, and spectroscopic experiments. TD performed all the live-cell imaging experiments. AS assisted with the synthesis and spectroscopic measurements. RB collected and analyzed single-crystal X-ray data. The manuscript was written from the inputs from all authors. All authors have participated in analyzing the data presented in the manuscript. All the experiments were performed and the project was completed under the guidance of DC and ALK.

Conflicts of interest

There are no conflicts to declare.

Acknowledgements

We wish to acknowledge the financial support from the host institute IISER Bhopal. SB acknowledges fellowship support from UGC, India. TD and RB acknowledge doctoral fellowship support from IISERB. AS thanks the CSIR for his doctoral fellowship. We also thank NMR, the mass facility in the central instrumentation facility (CIF), and the departmental instrumentation facility at IISERB. We acknowledge the Department

of Science and Technology (DST), India, for the FIST support to our Biological Sciences Department at the IISERB for live-cell imaging facility.

Notes and references

1 C. de Duve, *Nat. Cell Biol.*, 2005, **7**, 847–849.
2 J. P. Luzio, P. R. Pryor and N. A. Bright, *Nat. Rev. Mol. Cell Biol.*, 2007, **8**, 622–632.
3 R. M. Perera and R. Zoncu, *Annu. Rev. Cell Dev. Biol.*, 2016, **32**, 223–253.
4 C. Settembre, A. Fraldi, D. L. Medina and A. Ballabio, *Nat. Rev. Mol. Cell Biol.*, 2013, **14**, 283–296.
5 R. E. Lawrence and R. Zoncu, *Nat. Cell Biol.*, 2019, **21**, 133–142.
6 B. Liu, H. Du, R. Rutkowski, A. Gartner and X. Wang, *Science*, 2012, **337**, 351.
7 G. A. Wyant, M. Abu-Remaileh, R. L. Wolfson, W. W. Chen, E. Freinkman, L. V. Danai, M. G. Vander Heiden and D. M. Sabatini, *Cell*, 2017, **171**, 642–654.e612.
8 Q. Verdon, M. Boonen, C. Ribes, M. Jadot, B. Gasnier and C. Sagné, *Proc. Natl. Acad. Sci. U. S. A.*, 2017, **114**, E3602.
9 J. R. Casey, S. Grinstein and J. Orlowski, *Nat. Rev. Mol. Cell Biol.*, 2010, **11**, 50–61.
10 J. Zhao, S. Benlekbir and J. L. Rubinstein, *Nature*, 2015, **521**, 241–245.
11 C. Settembre, R. Zoncu, D. L. Medina, F. Vetrini, S. Erdin, S. Erdin, T. Huynh, M. Ferron, G. Karsenty, M. C. Vellard, V. Facchinetti, D. M. Sabatini and A. Ballabio, *EMBO J.*, 2012, **31**, 1095–1108.
12 B. Turk and V. Turk, *J. Biol. Chem.*, 2009, **284**, 21783–21787.
13 F. M. Platt, A. d'Azzo, B. L. Davidson, E. F. Neufeld and C. J. Tifft, *Nat. Rev. Dis. Primers*, 2018, **4**, 27.
14 E. B. Vitner, F. M. Platt and A. H. Futerman, *J. Biol. Chem.*, 2010, **285**, 20423–20427.
15 S. Jäger, C. Bucci, I. Tanida, T. Ueno, E. Kominami, P. Saftig and E.-L. Eskelinen, *J. Cell Sci.*, 2004, **117**, 4837.
16 L. Jahreiss, F. M. Menzies and D. C. Rubinsztein, *Traffic*, 2008, **9**, 574–587.
17 S. Kimura, T. Noda and T. Yoshimori, *Autophagy*, 2007, **3**, 452–460.
18 L. Yu, C. K. McPhee, L. Zheng, G. A. Mardones, Y. Rong, J. Peng, N. Mi, Y. Zhao, Z. Liu, F. Wan, D. W. Hailey, V. Oorschot, J. Klumperman, E. H. Baehrecke and M. J. Lenardo, *Nature*, 2010, **465**, 942–946.
19 X. Zhang, L. Wang, B. Lak, J. Li, E. Jokitalo and Y. Wang, *Dev. Cell*, 2018, **45**, 245–261.e246.
20 S. S. Li, M. Zhang, J. H. Wang, F. Yang, B. Kang, J. J. Xu and H. Y. Chen, *Anal. Chem.*, 2019, **91**, 8398–8405.
21 K. Todkar, H. S. Ilamathi and M. Germain, *Front. Cell Dev. Biol.*, 2017, **5**, 1–7.
22 A. D. Klein and A. H. Futerman, *Pediatr Endocrinol Rev*, 2013, **11**(suppl. 1), 59–63.
23 C. Nilsson, K. Kågedal, U. Johansson and K. Öllinger, *Methods Cell Sci*, 2004, **25**, 185–194.
24 A. Ballabio and J. S. Bonifacino, *Nat. Rev. Mol. Cell Biol.*, 2020, **21**, 101–118.
25 B. Cabukusta and J. Neefjes, *Traffic*, 2018, **19**, 761–769.
26 X. Zhang, C. Wang, Z. Han and Y. Xiao, *ACS Appl. Mater. Interfac.*, 2014, **6**, 21669–21676.
27 Z. Yang, J. Cao, Y. He, J. H. Yang, T. Kim, X. Peng and J. S. Kim, *Chem. Soc. Rev.*, 2014, **43**, 4563–4601.
28 J. P. Luzio, Y. Hackmann, N. M. G. Dieckmann and G. M. Griffiths, *Cold Spring Harbor Perspect. Biol.*, 2014, **6**, a016840.
29 F. M. Platt, *Nature*, 2014, **510**, 68–75.
30 J. A. Mindell, *Annu. Rev. Physiol.*, 2012, **74**, 69–86.
31 D. Shi, L. Hu, X. Li, W. Liu, Y. Gao, X. Li, B. Jiang, C. Xia, Y. Guo and J. Li, *Sens. Actuators, B*, 2020, **319**, 128302.
32 H. Xiao, P. Li and B. Tang, *Coord. Chem. Rev.*, 2021, **427**, 213582.
33 L. Fan, X. Wang, J. Ge, F. Li, X. Wang, J. Wang, S. Shuang and C. Dong, *Chem. Commun.*, 2019, **55**, 4703–4706.
34 M. Li, J. Fan, H. Li, J. Du, S. Long and X. Peng, *Biomaterials*, 2018, **164**, 98–105.
35 Z. Li, S. Wu, J. Han and S. Han, *Analyst*, 2011, **136**, 3698–3706.
36 H. M. Kim, M. J. An, J. H. Hong, B. H. Jeong, O. Kwon, J.-Y. Hyon, S.-C. Hong, K. J. Lee and B. R. Cho, *Angew. Chem., Int. Ed.*, 2008, **47**, 2231–2234.
37 J. Chan, S. C. Dodani and C. J. Chang, *Nat. Chem.*, 2012, **4**, 973–984.
38 P. Gao, W. Pan, N. Li and B. Tang, *Chem. Sci.*, 2019, **10**, 6035–6071.
39 X. Shi, N. Yan, G. Niu, S. H. P. Sung, Z. Liu, J. Liu, R. T. K. Kwok, J. W. Y. Lam, W.-X. Wang, H. H. Y. Sung, I. D. Williams and B. Z. Tang, *Chem. Sci.*, 2020, **11**, 3152–3163.
40 W. Xu, Z. Zeng, J.-H. Jiang, Y.-T. Chang and L. Yuan, *Angew. Chem., Int. Ed.*, 2016, **55**, 13658–13699.
41 L. Yuan, L. Wang, B. K. Agrawalla, S.-J. Park, H. Zhu, B. Sivaraman, J. Peng, Q.-H. Xu and Y.-T. Chang, *J. Am. Chem. Soc.*, 2015, **137**, 5930–5938.
42 P. Ning, W. Wang, M. Chen, Y. Feng and X. Meng, *Chinese Chem. Lett.*, 2017, **28**, 1943–1951.
43 H. Zhu, J. Fan, Q. Xu, H. Li, J. Wang, P. Gao and X. Peng, *Chem. Commun.*, 2012, **48**, 11766–11768.
44 H. Zhu, J. Fan, J. Du and X. Peng, *Acc. Chem. Res.*, 2016, **49**, 2115–2126.
45 K. P. Carter, A. M. Young and A. E. Palmer, *Chem. Rev.*, 2014, **114**, 4564–4601.
46 I. D. Johnson and T. Z. M. Spence, *Molecular Probes Handbook: A Guide to Fluorescent Probes and Labeling Technologies*, Life Technologies Corporation, 11th edn, 2010.
47 G. Signore, R. Nifosì, L. Albertazzi, B. Storti and R. Bizzarri, *J. Am. Chem. Soc.*, 2010, **132**, 1276–1288.
48 K. Pal, I. Samanta, R. K. Gupta, D. Goswami and A. L. Koner, *Chem. Commun.*, 2018, **54**, 10590–10593.
49 T. Dutta, K. Pal and A. L. Koner, *Sci. Rep.*, 2020, **10**, 4166.
50 D. M. Chudakov, M. V. Matz, S. Lukyanov and K. A. Lukyanov, *Physiol. Rev.*, 2010, **90**, 1103–1163.
51 X. Li, X. Gao, W. Shi and H. Ma, *Chem. Rev.*, 2014, **114**, 590–659.

52 S. Biswas, V. Sharma, P. Kumar and A. L. Koner, *Sens. Actuators, B*, 2018, **260**, 460–464.
53 W. Luo, H. Jiang, X. Tang and W. Liu, *J. Mater. Chem. B*, 2017, **5**, 4768–4773.
54 F. Tanaka, H. Chosrowjan, S. Taniguchi, N. Mataga, K. Sato, Y. Nishina and K. Shiga, *J. Phys. Chem. B*, 2007, **111**, 5694–5699.
55 R. M. Duke, E. B. Veale, F. M. Pfeffer, P. E. Kruger and T. Gunnlaugsson, *Chem. Soc. Rev.*, 2010, **39**, 3936–3953.
56 N. Meher and P. K. Iyer, *Angew. Chem., Int. Ed.*, 2018, **57**, 8488–8492.
57 R. F. W. Bader, *Atoms in Molecules: A Quantum Theory*, Oxford University Press, Oxford, U.K., 1990.
58 P. L. Popelier, *Atoms in Molecules: An Introduction*, Prentice Hall, London, 2000.
59 T. A. Keith, *TK Gristmill 19.10.12*, Overland Park KS, USA, 2019.
60 E. Y. Tupikina, M. Sigalov, I. G. Shenderovich, V. V. Mulloyarova, G. S. Denisov and P. M. Tolstoy, *J. Chem. Phys.*, 2019, **150**, 114305.
61 D. Magde, R. Wong and P. G. Seybold, *Photochem. Photobiol.*, 2002, **75**, 327–334.
62 J. Fan, Z. Han, Y. Kang and X. Peng, *Sci. Rep.*, 2016, **6**, 19562.
63 Z. R. Grabowski, K. Rotkiewicz and W. Rettig, *Chem. Rev.*, 2003, **103**, 3899–4032.
64 R. Greiner, T. Schlücker, D. Zgela and H. Langhals, *J. Mater. Chem. C*, 2016, **4**, 11244–11252.
65 C. Reichardt and T. Welton, in *Solvents and Solvent Effects in Organic Chemistry*, Wiley VCH, 3rd edn, 2010, pp. 425–508.
66 A. Kawai, H. Uchiyama, S. Takano, N. Nakamura and S. Ohkuma, *Autophagy*, 2007, **3**, 154–157.
67 X. D. Wang, L. Fan, Y. B. Wang, C. H. Zhang, W. T. Liang, S. M. Shuang and C. Dong, *J. Mater. Chem. B*, 2020, **8**, 1466–1471.
68 W. W. Y. Yim and N. Mizushima, *Cell Discov*, 2020, **6**, 1–12.
69 M. Mauthe, I. Orhon, C. Rocchi, X. D. Zhou, M. Luhr, K. J. Hijlkema, R. P. Coppes, N. Engedal, M. Mari and F. Reggiori, *Autophagy*, 2018, **14**, 1435–1455.
70 B. L. Sprague, R. L. Pego, D. A. Stavreva and J. G. McNally, *Biophys. J.*, 2004, **86**, 3473–3495.
71 M. Kang, C. A. Day, K. Drake, A. K. Kenworthy and E. DiBenedetto, *Biophys. J.*, 2009, **97**, 1501–1511.
72 D. M. Soumpasis, *Biophys. J.*, 1983, **41**, 95–97.
73 M. Kang, C. A. Day, A. K. Kenworthy and E. DiBenedetto, *Traffic*, 2012, **13**, 1589–1600.
74 X. Zheng, W. Zhu, F. Ni, H. Ai, S. Gong, X. Zhou, J. L. Sessler and C. Yang, *Chem. Sci.*, 2019, **10**, 2342–2348.
75 J. Yin, M. Peng and W. Lin, *Chem. Commun.*, 2019, **55**, 11063–11066.
76 K. Pal, P. Kumar and A. L. Koner, *J. Photochem. Photobiol. B*, 2020, 206.
77 R. Edmondson, J. J. Broglie, A. F. Adcock and L. J. Yang, *Assay Drug Dev Techn*, 2014, **12**, 207–218.
78 K. Pal, A. Sharma and A. L. Koner, *Org. Lett.*, 2018, **20**, 6425–6429.
79 G. de Voer, D. Peters and P. E. M. Taschner, *BBA, Mol. Basis Dis.*, 2008, **1782**, 433–446.
80 H. C. Roh, S. Collier, J. Guthrie, J. D. Robertson and K. Kornfeld, *Cell Metab.*, 2012, **15**, 88–99.
81 E. C. Dell'Angelica, C. Mullins, S. Caplan and J. S. Bonifacino, *FASEB J.*, 2000, **14**, 1265–1278.